A DEM-based heat transfer model for the evaluation of effective thermal conductivity of packed beds filled with stagnant fluid: Thermal contact theory and numerical simulation

Lei Chen [a,b], Cong Wang [a,c], Marigrazia Moscardini [b], Marc Kamlah [b], Songlin Liu [a,*]

[a] *Institute of Plasma Physics, Chinese Academy of Sciences (ASIPP), Hefei, Anhui 230031, China*
[b] *Institute for Applied Materials (IAM-WBM), Karlsruhe Institute of Technology (KIT), 76344 Eggenstein-Leopoldshafen, Germany*
[c] *University of Science and Technology of China, Hefei, Anhui 230027, China*

ABSTRACT

The Effective thermal conductivity (k_{eff}) is one of the key thermal properties for packed beds in the presence of a stagnant fluid. In this study, a thermal discrete element model (*DEM*) based on the original Cheng-Yu-Zulli analytical model for mono-sized packed beds has been improved and implemented especially for mixed beds of different particle sizes or materials. In order to perform the DEM simulation for packed beds, a thermal contact theory considering three heat transfer mechanisms (solid contact conduction, solid-fluid-solid conduction and radiation) was derived and applied in the network of Voronoi cells obtained by radical Voronoi tessellation of the relevant beds. The numerical model was validated through a comparison with experimental results already reported in literature and a good prediction for the effective thermal conductivity was obtained for both mono-sized and multi-sized packed beds in a wide range of solid-to-fluid conductivity ratio. The model also showed a good performance to study the heat flow distribution as well as the coupled thermo-mechanical behavior of packed beds.

© 2018 Elsevier Ltd. All rights reserved.

1. Introduction

Packed beds have been widely used in various thermal energy systems such as catalytic reactors [1], heat exchangers [2], and high temperature gas-cooled reactors (*HTGR*) [3,4], and they are under consideration for the solid breeding blankets for fusion reactors [5,6], Thermal properties, especially the effective thermal conductivity (k_{eff}), are key parameters with regard to heat transfer in packed beds. A variety of previous experimental research studies [7–13], theoretical models [14–20] and numerical simulations [21–26] have been performed to obtain k_{eff} of packed beds. Concerning experiments, the majority of the research [10–13] focused on pebble beds of a single particle material due to their wide applications, but only limited data were measured for mixed pebble beds with different materials [8,9]. Besides, less experiments [7–9] were reported on binary pebble beds with different particle sizes. In regard to theoretical models, most of the researchers, such as Kunii and Smith [14], Bauer et al. (the ZBS model) [15], and Hall and Martin [16] estimated k_{eff} based on the heat transfer analysis within a representative cell for unitary, i.e. mono-sized pebble

beds of a single material. Although these semi-empirical formulas have successfully predicted good results for k_{eff}, they are not applicable for mixed beds of different materials and are probably not accurate enough for multi-sized or polydisperse pebble beds due to their complex packing structures. The thought of representative cell model was further improved by Cheng et al. [18] and Hsu et al. [17] to illustrate periodic porous structures composed of arrays of touching composite materials with various shapes. Their models were found effective in a wide range of solid-to-fluid conductivity ratio up to 10,000. More recently, Van Antwerpen et al. [20] proposed a multi-sphere unit cell model considering the conduction and radiation heat transfer mechanisms to reflect the influence of local packing structures on k_{eff}. More theoretical models were summarized by Cheng et al. [18] and Van Antwerpen et al. [19]. Besides, various numerical models based on volume average method [21], unit cell approach [22], DEM method [24,26,27], and CFD-DEM method [4,25] were also introduced to predict k_{eff} of pebble beds. In recent years, the influence of the pebble bed packing structure has been considered in the heat transfer modeling in many studies. Cheng et al. (called Cheng-Yu-Zulli model in the present study) [23,28] estimated k_{eff} for mono-sized pebble beds by using Voronoi tessellation. Namely, in their model, the nominal heat transfer area of a contact pair is given by Voronoi

---

Nomenclature

A	dimensionless quantity in Eq. (14), [–]
A_m	effective heat transfer area of a contact, [m^2]
A_i, A_j	radiant exchange areas of surfaces on the corresponding spheres, [m^2]
$A_{i'}, A_{j'}$	projective area of A_i, A_j, [m^2]
A_n	nominal heat transfer area of a contact, [m^2]
A_w	area of the top wall, [m^2]
B	dimensionless quantity in Eq. (14), [–]
c_i, c_j	$c_i = R_{ci}/R_i$, $c_j = R_{cj}/R_j$, [–]
C_{pi}	specific heat capacity of particle i, [W/kg/K]
d_p	particle diameter, [m]
E_e	equivalent modulus, [Pa]
E_i, E_j	Young's modulus of particle i or j, [Pa]
F_n	normal contact force, [N]
$F_{ij}, F_{iR}, F_{jR}\ F_{i'j'}, F_{i'j}, F_{ij'}$	view factor between corresponding surfaces, [–]
$H_{ij}^t, H_{ij}^d, H_{ij}^r$	effective heat conductance of a thermal contact/contact/conduction/radiation part, [W/K]
$H_m, \bar{H}_m, H_{ij}$	effective heat conductance of a contact, [W/K]
k_m	effective conductivity in contact, [W/m/K]
k_{eff}	effective thermal conductivity, [W/m/K]
k_f, k_g	fluid/gas conductivity, [W/m/K]
k_{xx}, k_{yy}, k_{zz}	corresponding components of the k_{eff} tensor, [W/m/K]
k_s, k_{si}, k_{sj}	solid conductivity of particles, [W/m/K]
K_{si}, K_{sj}	dimensionless solid conductivity, [–]
L_m	contact length, [m]
$L_{ij}, L_{i'j'}$	contact length/distance between surface i' and j', [m]
M_i	mass of particle i, [kg]
$n_m, \bar{n}_m$	contact number on a particle/average coordination number, [–]
N_m, N_p, N_{pw}	total contact number/particle number within a packed bed/contacted with top wall, [–]
$\Delta N_{m\varphi}$	contact number in $\varphi \sim \varphi + \Delta\varphi$ direction, [–]
$\hat{n}_{q,m}, \hat{n}_{L,m}$	unit vector along the direction of q or L, [–]
P	pressure, [Pa]
P_0	initial mechanical load, [Pa]
P_f	packing factor, [–]
q, q_m	heat flux/heat flux within a contact, [W/m^2]
Q	total heat flow through all contacts, [W]
$Q_m, Q_{m\varphi}$	heat flow in a contact/in φ direction, [W]
ΔQ_φ	heat flow in $\varphi \sim \varphi + \Delta\varphi$ direction, [W]
Q_i	heat power in particle i, [W]
Q_{ij}, Q_{ji}	heat flow between particle i or j, [W]
$Q_{ij}^t, Q_{ji}^d, Q_{ji}^r$	contact/conduction/radiation heat flow, [W]
Q_{av}	average heat flow in contact, [W]
r	coordinate in radial direction, [m]
r_t	radius of a contact surface, [m]
R_e	equivalent radius, [m]
R_c, R_{ci}, R_{cj}	core radius of particle i or j, [m]
R_i, R_j	radius of smaller particle i or the larger j, [m]
$R_{i'}, R_{j'}$	projective radius of surface i' or j', [m]
T	temperature, [K]
T_i, T_j	core temperature of particle i or j, [K]
T_θ	fluid temperature at Point P on the rotational hyperboloid, [K]
$T_{\theta i}, T_{\theta j}$	surface temperature of particle i or j, [K]
V	volume of a packed bed, [m^3]
X, X_{min}, X_{max}	dimensionless quantity in Eq. (17), [–]
$Y_1, Y_2,$	dimensionless quantity in Eq. (16), [–]
x, y, z	coordinate, [m]

Greek symbols

α_i, α_j	$\alpha_i = R_i/L_{ij}$, $\alpha_j = R_j/L_{ij}$, [–]
$\Delta\alpha$	$\Delta\alpha = \alpha_j - \alpha_i$, [–]
δ_i, δ_j	$\delta_i = \rho_i/L_{ij}$, $\delta_j = \rho_j/L_{ij}$, [–]
$\delta_{imax}, \delta_{jmax}$	maximum value of δ_i, δ_j, [–]
δ_n	normal overlap, [m]
ε	$\varepsilon = R_j/R_i \geqslant 1$, radius ratio, [–]
$\varepsilon_{ri}, \varepsilon_{rj}$	emissivity of particles i or j, [–]
θ_i, θ_j	angle from the central axis of a contact, [rad]
θ_{im}, θ_{jm}	maximum angle of θ_i, θ_j, [rad]
Λ	discriminant for the integration of Eq. (13), [–]
v_i, v_j	Poisson's ratio of particle i or j, [–]
ρ_i, ρ_j	distance away from the center of particle i or j, [m]
σ	the Stephan-Boltzmann constant, 5.67×10^{-8} [W/m^2/K^4]
τ	time, [s]
φ	contact angle, [rad]

Superscripts and Subscripts

t, d, r	contact, conduction, radiation
m	thermal contact
e	equivalent
eff	effective
f, g	fluid, gas
i, j	particle No.
max, min	maximum, minimum
n	normal/nominal
s	solid

Abbreviations

CFD	computational fluid dynamics
DEM	discrete element method
HTGR	high temperature gas-cooled reactor
PDF	probability density function
ZBS	Zehner-Bauer-Schlünder

tessellation for the mono-sized bed. Therefore, the calculated k_{eff} reflects the impact of packing structure. Wu et al. [4] also utilized Voronoi tessellation in their CFD-DEM simulation work taking into account the radiation heat transfer, which is essential for the packed fuel pebbles of about 60 mm used in HTGR at a high temperature (about 1100 K). Moscardini et al. [26] and Gan et al. [27] improved the original Batchelor and O'Brien's analytical model [29] and developed an in-house thermal DEM code for fusion breeding blanket pebble beds. The thermal DEM code can be applied to unitary, binary, and polydisperse pebble beds, but radiation heat transfer is not implemented as the relevant pebble beds are composed of very small particles with a range of about 0.3–1.2 mm and in that case the radiation effect can be neglected [26]. All the above numerical studies made significant progress and have proven that the DEM method is a promising approach to simulate the heat transfer and fluid flow of fixed or fluidized beds. However, further studies are still necessary to improve the reliability of the DEM models and extend the applicable field. Therefore, in this study the original Cheng-Yu-Zulli model for mono-sized bed was extended to account for packed beds consisting of different particle sizes or materials and implemented into a DEM code running in the PFC software [30]. The solid contact con-

duction, solid-fluid-solid conduction, and radiation are considered in the current thermal DEM model as the main heat transfer mechanisms in packed beds with stagnant fluid.

In this paper, Section 2 describes the thermal contact theory implemented by the DEM approach and the numerical methodology to predict k_{eff} of pebble beds. Results and discussions are presented in Section 3, while the conclusions are reported in Section 4.

2. Methodology

2.1. Heat transfer modeling by DEM approach

In recent years, the DEM method has been utilized to simulate the heat transfer characteristics of packed beds [4,26,27,31]. Since the pebble bed is usually a mixture of solid particles and surrounding flowing fluid, an accurate heat transfer model for the pebble bed will be very complex. One possible assumption is that each individual particle i has a characteristic temperature T_i. Therefore, the heat transfer equation of particle i can be simplified to

$$M_i C_{pi} \frac{dT_i}{d\tau} = \sum_{j=1}^{n_m} Q_{ji} + Q_i, \qquad (1)$$

where M_i and C_{pi} are the particle mass and specific heat capacity, respectively, Q_i denotes the volume heat power coming from the inner heating and can be estimated by a volume average method [27], while Q_{ji} is the heat flow transferred through each neighboring particle j. Then Q_{ji} is summed over all the n_m particles adjacent to particle i. As a consequence, heat transfer of the whole granular system is calculated from a system of linear equations for all the particles as well as additional thermal equations describing initial settings and boundary conditions. But before that, the unknown Q_{ji} should be determined by a thermal contact model which is similar to the mechanical contact model defined in DEM models.

Fig. 1 shows the flow diagram for the current DEM simulation. In the mechanical DEM simulation, the pebble bed assemblies are created by a previous self-developed mechanical DEM code [32] running in PFC [30]. One or several groups of spherical particles with the specified size distribution and material properties are randomly initialized in a pre-defined container with rigid walls or periodic boundaries. Huge overlaps may exist between these particles, which induces large repulsive contact forces.

Therefore, these overlapping pebbles move away from each other and eventually reach a static equilibrium state. Meanwhile the positions of lateral walls or periodic boundaries are adjusted through a control scheme as in a servo hydraulic machine until the mean stress of the assembly is close to the initial mechanical load P_0 [32]. As examples, a mono-sized bed with rigid walls and a multi-sized bed with periodic boundaries for the lateral sides and flat top and bottom walls are shown in Fig. 2(a) and Fig. 2(b), respectively. A given Gaussian distribution shown in Fig. 2(c) is assumed for the multi-sized case. In both cases, the Hertz-Mindlin mechanical contact model is used to calculate the particle-particle or particle-wall contact forces. Virtual ghost particles are generated in PFC to transfer the contact force between particles nearby the periodic boundaries.

In the subsequent thermal DEM simulation, the pebble bed assembly is reloaded to perform the heat transfer simulation. During this process, Eq. (1) is discretized by expressing the time derivative using forward finite differences defined in PFC [30], and the thermal timestep is adjusted to achieve the numerical stability of the explicit scheme. The user-defined thermal contact model, which defines the heat flow between adjacent particles (or ghost particles in case of periodic boundaries), is implemented by a C++ code and then compiled as an executable DLL (Dynamic Link Library) file running in PFC. Once the average ratio of the unbalanced to total heat power for all particles is lower than 10^{-4}, the granular system is supposed to reach the steady-state temperature field. The temperature distribution under certain thermal boundary conditions can be used to compute the effective thermal conductivity and thus validate the thermal DEM model.

In order to capture the influence of the packing structure on heat transfer of mono-sized pebble beds, Cheng et al. [23,28] and Wu et al. [4] introduced Voronoi tessellation. By this method, the considered bed (pebbles and void space) is divided into Voronoi polyhedrons containing single pebbles individually. This work extends the Cheng-Yu-Zulli model to the case of polydisperse pebble beds by using the radical Voronoi tessellation algorithm [33] implemented in a C++ library. Fig. 2(a) and (b) also show the Voronoi tessellations for the above cases of pebble beds. Two neighboring Voronoi polyhedrons coming from the multi-sized pebble bed assembly are shown in Fig. 2(d). The two Voronoi cells have a common polygonal surface with a nominal area of A_n. For simplicity, the common polygon is assumed to be equivalent to a
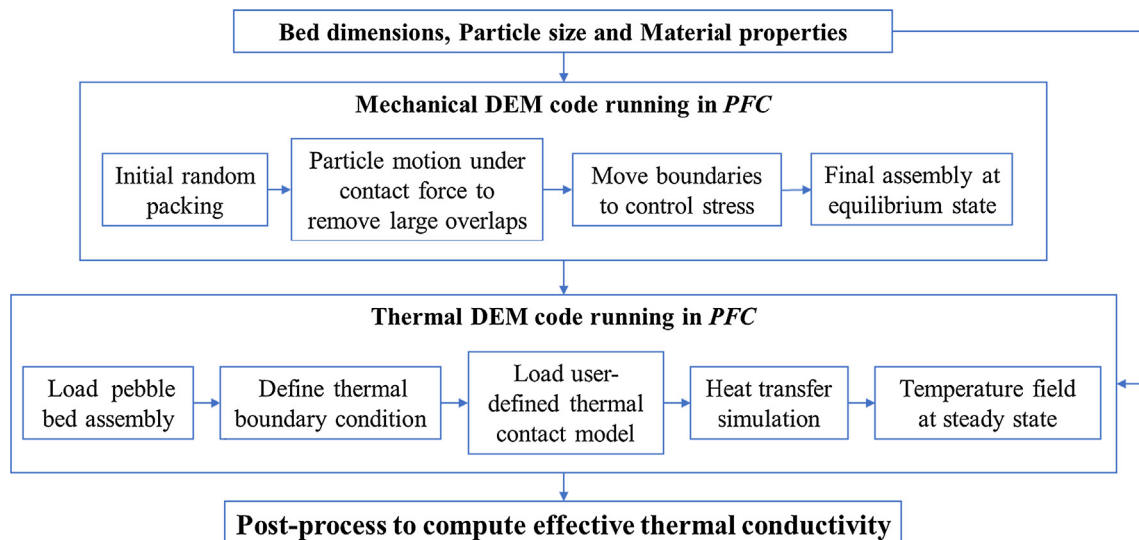

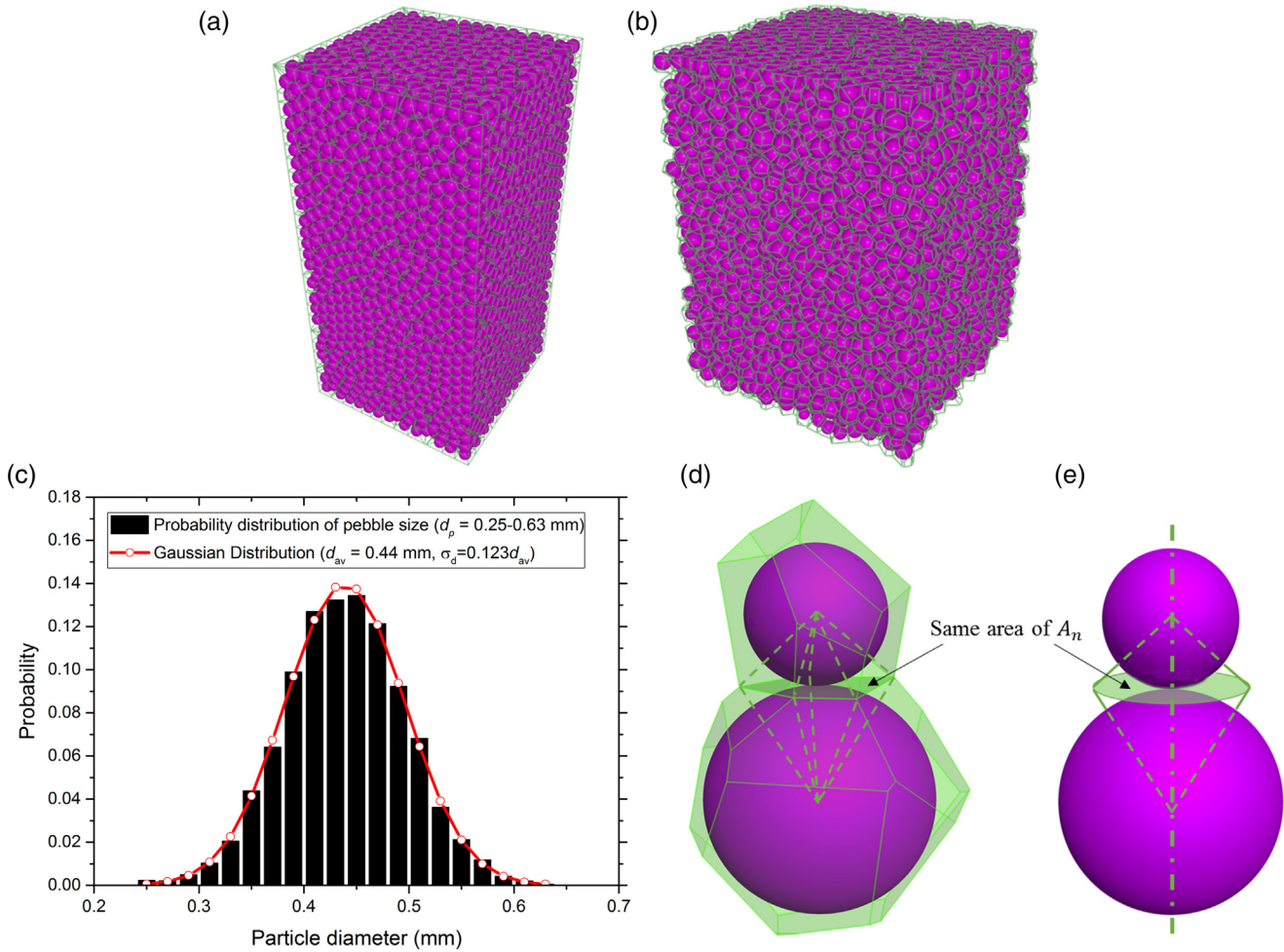**Fig. 1.** Flow diagram for the current DEM simulation.

Fig. 2. Assemblies of the pebble beds and their Voronoi tessellations. (a) Mono-sized bed in a rigid structure; (b) Multi-sized bed with top/bottom walls and lateral periodic boundary; (c) Pebble size distribution in the multi-sized bed; (d) Two neighboring Voronoi cells; (e) A double-cone model. The double-cone represents one thermal contact.

circular surface (shown in Fig. 2(e)) with the same area A_n and heat flow between the two particles is assumed to pass through the circular double-cone zone only. Similar assumptions have been made by Cheng et al. [33] to study the heat transfer of mono-sized beds.

2.2. Thermal contact model

In general, Q_{ji} in Eq. (1) can be expressed as

$$Q_{ji} = -Q_{ij} = -H_{ij}(T_i - T_j), \tag{2}$$

where H_{ij} is the effective heat conductance [W/K] between particles i and j. Yagi and Kunni [7] summarized the heat transfer mechanisms in fluid-filled packed beds: (1) heat conduction through the solid and fluid phase; (2) heat conduction through the contact area of solid; (3) radiant heat transfer between solid surfaces (in case of gas); (4) radiant heat transfer between adjacent voids (in case of gas); (5) convective heat transfer, including the solid-fluid convection and the fluid mixing convection. However, for packed beds filled with a stagnant fluid, only the first three dominant mechanisms will be initially considered in the current work. Therefore, the effective heat conductance can be rewritten as

$$H_{ij} = H_{ij}^t + H_{ij}^d + H_{ij}^r, \tag{3}$$

where H_{ij} includes the solid contact conduction part H_{ij}^t, the solid-fluid-solid conduction part H_{ij}^d and the radiation part H_{ij}^r. It is noted

that thermal contacts between adjacent particles with separating gaps should also be considered because the solid-fluid-solid conduction and the radiation part still exist even though in this situation the solid contact part has no contribution.

2.2.1. Solid contact conduction

Solid contact conduction exists between two touching particles with a contact area, as shown in Fig. 3(a). As reported in literatures [29,34], the temperature distribution in the near-contact region is significantly different from that far away from the contact region, which indicates that solid contact conduction must be considered. Batchelor and O'Brien [29] proposed an approximate analytical solution for the effective heat conductance H_{ij}^t between two smooth elastic spheres with a contact surface of radius r_t (determined by Hertzian contact theory), which is also used by [26,23] and written as

$$H_{ij}^t = 2r_t k_s = \frac{4\sqrt{R_e \delta_n}}{1/k_{si} + 1/k_{sj}} = \frac{4}{1/k_{si} + 1/k_{sj}} \left(\frac{3F_n R_e}{4E_e} \right)^{1/3} \tag{4}$$

with

$$E_e = \left(\frac{1 - v_i^2}{E_i} + \frac{1 - v_j^2}{E_j} \right)^{-1}, R_e = \left(\frac{1}{R_i} + \frac{1}{R_j} \right)^{-1}, \text{ and}$$

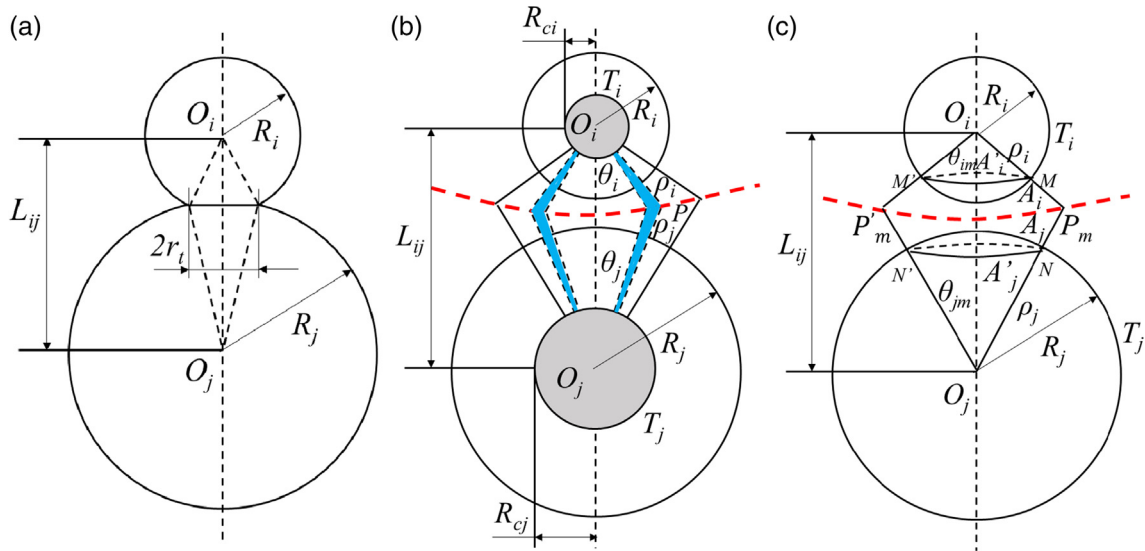$$\delta_n = R_i + R_j - L_{ij}, \tag{5}$$

Fig. 3. Thermal contact model for two adjacent particles. (a) solid contact conduction part; (b) solid-fluid-solid conduction part; (c) radiation part.

where k_s, υ, E and R are the particle conductivity, Poisson's ratio, Young's modulus and radius, respectively, and with subscript i and j indicating the corresponding particle number. F_n denotes the normal contact force induced by the normal overlap δ_n. E_e and R_e are the equivalent modulus and radius defined by the Hertzian contact theory. Note that the solid conductivity k_s in Eq. (4) has been replaced with $2k_{si}k_{sj}/(k_{si}+k_{sj})$ to consider particles with different thermal properties. Eq. (4) shows the relationship between the conductance and the contact force, which enables the current model to estimate the impact of an external mechanical load on the effective thermal conductivity.

2.2.2. Solid-fluid-solid conduction

In most of the fluid-filled packed beds, the solid phase has a larger thermal conductivity than the fluid phase, which means the temperature distribution across the solid phase will be more uniform, especially in the central part of the particle. In view of that, Cheng et al. [23] assumed each particle had an isothermal core part of radius R_c and representative temperature. Following such a basic assumption, the temperature distribution of two adjacent equal-sized and multi-sized particles is solved numerically by using the commercial software COMSOL Multiphysics, as shown in Fig. 4. In both cases, the two particles of a unit temperature difference are surrounded by a stagnant fluid with a conductivity of k_f assuming to be $0.05k_s$, and the core part radius R_c, sketched in Fig. 4 by black circles within the particle boundaries, is assumed as half of the corresponding particle radius. For the equal-sized case, the two particles with the same radius of 3 mm have a small gap. while for the multi-sized case, the two particles have radii of 1 mm and 3 mm, respectively. As an approximation of the far-field boundary condition, the stagnant fluid is contained in a large zone with a radius of 30 times of the maximum particle radius. For the equal-sized particles, heat flux indicated by the black flowlines flows from the higher-temperature particle centroid to the lower-temperature particle centroid, passing through a Point P equidistant from both particle surfaces. For simplicity, Cheng
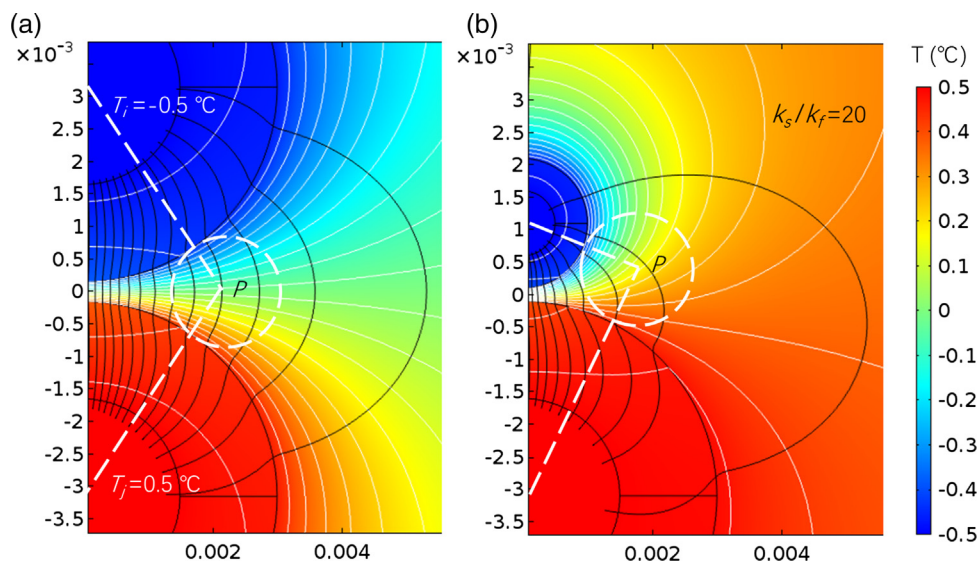

Fig. 4. Temperature distribution of two adjacent particles. (a) equal-sized particles; (b) multi-sized particles. The white lines indicate the isothermal surfaces and the black lines perpendicular to the white lines represent the heat flowlines.

et al. [23] supposed that the approximate heat flux path for two equal-sized particles is along the dashed polyline shown in Fig. 4 (a). A similar heat flux path is now introduced here for the multi-sized particle pair, but Point P might deviate from the middle virtual plane. As shown in Fig. 4(b), we assume in this situation Point P still has the same distance to both particle surfaces, which means Point P is located on a rotational hyperboloid with both particle centroids as the focal points and the central axis of the contact pair as the rotation axis. It is noted that the hyperboloid turns into the middle virtual plane for the case of equal-sized particles.

Based on the above assumptions of an isothermal core and the heat flux path, heat flow dQ_{ij}^d through the infinitesimal volume within the smaller sphere shown in Fig. 3(b) is

$$dQ_{ij}^d = 2\pi r^2 \sin\theta_i d\theta_i \left(-k_{si}\frac{dT}{dr}\right) \text{ or } dT = \frac{dQ_{ij}^d}{2\pi k_{si}\sin\theta_i d\theta_i}\left(-\frac{dr}{r^2}\right). \quad (6)$$

Here, θ_i is the angle between the central axis and the investigated flow path (plotted in blue in Fig. 4), and r is the distance away from the corresponding particle centroid.

Integrating Eq. (6) from the boundary of the core part $(r = R_{ci}, T = T_i)$ to the boundary of the smaller particle $(r = R_i, T = T_{\theta,i})$, we obtain

$$T_i - T_{\theta,i} = \frac{dQ_{ij}^d}{2\pi k_{si}\sin\theta_i d\theta_i}\left(\frac{1}{R_{ci}} - \frac{1}{R_i}\right). \quad (7)$$

Similarly, analyses of the heat flow through outer fluid regions and the larger particle give equations

$$T_{\theta,i} - T_\theta = \frac{dQ_{ij}^d}{2\pi k_f\sin\theta_i d\theta_i}\left(\frac{1}{R_i} - \frac{1}{\rho_i}\right), \quad (8)$$

$$T_\theta - T_{\theta j} = \frac{dQ_{ij}^d}{2\pi k_f\sin\theta_j d\theta_j}\left(\frac{1}{R_j} - \frac{1}{\rho_j}\right), \quad (9)$$

$$T_{\theta j} - T_j = \frac{dQ_{ij}^d}{2\pi k_{sj}\sin\theta_j d\theta_j}\left(\frac{1}{R_{cj}} - \frac{1}{R_j}\right), \quad (10)$$

where ρ_i and ρ_j are the distances from Point P to the corresponding sphere centroid of the particles i and j, respectively. T_θ represents the fluid temperature at Point P on the rotational hyperboloid (Fig. 3(b)). Combining Eqs. (7), (8), (9) and (10)and rearranging the final equation, we get dQ_{ij}^d as

$$dQ_{ij}^d = \frac{2\pi k_f(T_i - T_j)}{\frac{1/R_{ci}-1/R_i}{K_{si}\sin\theta_i d\theta_i} + \frac{1/R_i-1/\rho_i}{\sin\theta_i d\theta_i} + \frac{1/R_j-1/\rho_j}{\sin\theta_j d\theta_j} + \frac{1/R_{cj}-1/R_j}{K_{sj}\sin\theta_j d\theta_j}} \quad (11)$$

with $K_{si} = k_{si}/k_f$ and $K_{sj} = k_{sj}/k_f$ denoting dimensionless solid conductivities of particles i and j, respectively. Appling the cosine law in triangle ΔO_iO_jP in Fig. 3(b) the following equations are obtained,

$$\cos\theta_i = \frac{\rho_i^2 + L_{ij}^2 - \rho_j^2}{2\rho_i L_{ij}} = \frac{1 - \Delta\alpha^2}{2\delta_i} - \Delta\alpha, \cos\theta_j = \frac{\rho_j^2 + L_{ij}^2 - \rho_i^2}{2\rho_j L_{ij}}$$
$$= \frac{1 - \Delta\alpha^2}{2(\delta_i + \Delta\alpha)} + \Delta\alpha, \quad (12a)$$

or the differential form as

$$\sin\theta_i d\theta_i = \frac{1 - \Delta\alpha^2}{2\delta_i^2}d\delta_i, \sin\theta_j d\theta_j = \frac{1 - \Delta\alpha^2}{2(\delta_i + \Delta\alpha)^2}d\delta_i, \quad (12b)$$

where $\delta_i = \rho_i/L_{ij}, \delta_j = \rho_j/L_{ij}, \alpha_i = R_i/L_{ij}, \alpha_j = R_j/L_{ij}$ and $\Delta\alpha = (\rho_j - \rho_i)/L_{ij} = (R_j - R_i)/L_{ij}$ are the dimensionless length for ρ_i, ρ_j, R_i, R_j and the particle radius difference, respectively. Substi-

tuting Eq. (12b) and the listed dimensionless variables into Eq. (11) yields

$$dQ_{ij}^d = \frac{\pi k_f L_{ij}(T_i - T_j)(1 - \Delta\alpha^2)d\delta_i}{(A + B)\delta_i^2 - 2(1 - \Delta\alpha B)\delta_i - (1 - \Delta\alpha B)\Delta\alpha}, \quad (13)$$

where

$$A = \frac{1}{\alpha_i K_{si}}\left(\frac{1}{c_i} - 1\right) + \frac{1}{\alpha_i}, B = \frac{1}{\alpha_j K_{sj}}\left(\frac{1}{c_j} - 1\right) + \frac{1}{\alpha_j},$$
$$c_i = R_{ci}/R_i, c_j = R_{cj}/R_j. \quad (14)$$

The integration of Eq. (13) will give

$$H_{ij}^d = \frac{Q_{ij}^d}{(T_i - T_j)} = \begin{cases} \frac{\pi k_f L_{ij}(1-\Delta\alpha^2)}{2\sqrt{|\Lambda|}}\ln\left|\frac{1-Y_1}{1+Y_1}\right|, \Lambda > 0 \\ \frac{\pi k_f L_{ij}(1-\Delta\alpha^2)}{A+B}\left(\frac{1}{\delta_{imin}} - \frac{1}{\delta_{imax}}\right), \Lambda = 0 \\ \frac{\pi k_f L_{ij}(1-\Delta\alpha^2)}{\sqrt{|\Lambda|}}\arctan Y_2, \Lambda < 0 \end{cases} \quad (15)$$

with

$$Y_1 = \frac{X_{max} - X_{min}}{1 - X_{max}X_{min}}, \quad Y_2 = \frac{X_{max} - X_{min}}{1 + X_{max}X_{min}}, \quad (16)$$

$$X_{max} = \frac{-1 + \Delta\alpha B + (A + B)\delta_{imax}}{\sqrt{|\Lambda|}}, X_{min} = \frac{-1 + \Delta\alpha B + (A + B)\delta_{imin}}{\sqrt{|\Lambda|}}, \quad (17)$$

where $\Lambda = (1 + \Delta\alpha A)(1 - \Delta\alpha B)$ represents the discriminant for the integration. Note that $\Lambda > 0$ can be simplified to $K_{sj} > (\varepsilon - 1)(1/c_j - 1)$. Considering $\varepsilon = R_j/R_i \geq 1$ and $c_j = R_{cj}/R_j < 1$, $\Lambda > 0$ is always true for the mono-sized bed. But for the multi-sized case, $\Lambda < 0$ is also possible if the conductivity ratio K_{sj} is not very high.

The upper limit of integral δ_{imax} can be linked to the nominal area A_n for the neighboring Voronoi cells shown in Fig. 2(d). According to the geometrical relationship, δ_{imax} can be expressed as

$$\delta_{imax} = \frac{1}{2}\left(\sqrt{1 + \frac{4A_n}{\pi L_{ij}^2(1 - \Delta\alpha^2)}} - \Delta\alpha\right). \quad (18)$$

The lower limit of integral δ_{imin} is determined by the particle contact state. For the situation of particles in mechanical contact, δ_{imin} is estimated to be

$$\delta_{imin} = \frac{1}{2}\left(\sqrt{1 + \frac{4r_t^2}{L_{ij}^2(1 - \Delta\alpha^2)}} - \Delta\alpha\right), \quad (19)$$

where the contact radius r_t can be solved from Eq. (4). For the non-contacting or point-contacting particles, r_t in Eq. (19) should be zero.

For the contact of equal-sized particles ($R_i = R_j$ and $\Delta\alpha = 0$), Eq. (15) gives a result consistent with Cheng-Yu-Zulli model [23].

2.2.3. Radiation heat transfer

Radiation is an important heat transfer mechanism for high-temperature packed beds. However, it is very difficult to predict the radiation heat transfer accurately due to the complex packing structures in the pebble beds. Cheng et al. [28] proposed a simplified radiation heat transfer model for mono-sized beds by adopting the following assumptions: (1) All particles are opaque spheres much larger than the radiation wavelength and the particle surfaces are gray emitting; (2) $\Delta T/T$ across a sphere layer is much less than unity; (3) Radiation heat transfer between two adjacent particles only exists in the virtual double-cone shown in Fig. 2(e) and the cones are enclosed by an imaginary re-radiating surface R (surface $MP_mNN'P_m'M'$ in Fig. 3(c)). This work follows the same

assumptions used in Cheng-Yu-Zulli model and extends it to the situation of multi-sized beds. Actually, Cheng et al. have given the radiative heat flow for adjacent Voronoi cells (see Fig. 3(c)) as

$$Q_{ij}^r = \frac{\sigma\left(T_i^4 - T_j^4\right)}{\frac{1-\varepsilon_{ri}}{\varepsilon_{ri}A_i} + \frac{1}{A_iF_{ij} + \left[1/(A_iF_{iR}) + 1/(A_jF_{jR})\right]^{-1}} + \frac{1-\varepsilon_{rj}}{\varepsilon_{rj}A_j}}, \tag{20}$$

where ε_{ri} and ε_{rj} are the emissivities of the related particles i and j, while $A_i = 2\pi R_i^2(1 - \cos\theta_i)$ and $A_j = 2\pi R_j^2(1 - \cos\theta_j)$ represent the radiant exchange areas of surfaces MM′ and NN′ on the corresponding spheres. F_{ij}, F_{iR}, and F_{jR} are the view factors of the surface pairs MM′ and NN′, MM′ and MP$_m$NN′P$'_m$M′, as well as NN′ and MP$_m$NN′P$'_m$M′, respectively.

By the reciprocity rule of the view factor,

$$A_iF_{iR} = A_i(1 - F_{ij}), \quad A_jF_{jR} = A_j(1 - F_{ji}) = A_j - A_iF_{ij}. \tag{21}$$

Substituting Eq. (21) into (20), we have

$$
\begin{aligned}
H_{ij}^r &= \frac{Q_{ij}^r}{(T_i - T_j)} = \frac{\sigma A_i\left(T_i^4 - T_j^4\right)/(T_i - T_j)}{\frac{1-\varepsilon_{ri}}{\varepsilon_{ri}} + \frac{1-\varepsilon_{rj}}{\varepsilon_{rj}A_j/A_i} + \frac{1 + A_j/A_i - 2F_{ij}}{A_j/A_i - F_{ij}^2}} \\
&\approx \frac{4\sigma A_i T_i^3}{\frac{1-\varepsilon_{ri}}{\varepsilon_{ri}} + \frac{1-\varepsilon_{rj}}{\varepsilon_{rj}A_j/A_i} + \frac{1 + A_j/A_i - 2F_{ij}}{A_j/A_i - F_{ij}^2}}
\end{aligned}
\tag{22}
$$

The approximation in Eq. (22) is reasonable if the particle temperature difference is small enough. For mono-sized particles with the same material properties, $\varepsilon_{rj} = \varepsilon_{rj}, A_i = A_j$. Therefore, in this case

$$H_{ij}^r = \frac{\sigma A_i\left(T_i^4 - T_j^4\right)/(T_i - T_j)}{2\left(\frac{1-\varepsilon_{ri}}{\varepsilon_{ri}} + \frac{1}{1+F_{ij}}\right)} \approx \frac{4\sigma A_i T_i^3}{2\left(\frac{1-\varepsilon_{ri}}{\varepsilon_{ri}} + \frac{1}{1+F_{ij}}\right)}. \tag{23}$$

This is in accordance with the equation given by Cheng-Yu-Zulli model [28]. Cheng et al. determined the view factor F_{ij} in Eq. (23) by a numerical method. Actually, an analytical solution can be obtained by further derivation.

The view factor from A_i to A_j is actually equal to that from A_i to A'_j (the projected surface of A_j in the vertical direction). This is because any ray of radiant energy emanating from A_i and striking A_j will also strike A'_j and vice versa – if it strikes A'_j it will also strike A_j. Together with the reciprocity rule, we have

$$F_{ij} = F_{ij'} = \frac{A'_i}{A_i}F_{i'j'} = \frac{1 + \cos\theta_{im}}{2}F_{i'j'}, \tag{24}$$

where $F_{i'j'}$ is the view factor between the two coaxial circular planes A'_i (projected surface of A_i) and A'_j with a vertical distance of $L_{i'j'} = L_{ij} - R_i\cos\theta_{im} - R_j\cos\theta_{jm}$. According to [35],

$$F_{i'j'} = \frac{1}{2}\left(z - \sqrt{z^2 - \frac{4R_j'^2}{R_i'^2}}\right) \tag{25}$$

with

$$z = 1 + \frac{4R_j'^2}{R_i'^2} + \frac{L_{i'j'}^2}{R_i'^2}, \tag{26}$$

$$\cos\theta_{im} = \frac{1 - \Delta\alpha^2}{2\delta_{imax}} - \Delta\alpha, \quad \cos\theta_{jm} = \frac{1 - \Delta\alpha^2}{2(\delta_{imax} + \Delta\alpha)} + \Delta\alpha, \tag{27}$$

where $R'_i = R_i\sin\theta_{im}$ and $R'_j = R_j\sin\theta_{jm}$ are the radius of A'_i and A'_j, respectively. For particles in mechanical contact, the central contacting part will have no radiant exchange, but this effect is neglected due to the limited fraction of the mechanical contact area in the total heat exchange area.

2.3. Effective thermal conductivity

In this work the effective thermal conductivity k_{eff} at a certain temperature is evaluated by the thermal DEM simulation in a representative rectangular assembly of a packed bed with a small temperature difference between the top and bottom walls as follows. As shown in Fig. 5(a), in the thermal DEM simulation, the bottom layer of particles is kept as a constant temperature T_w, while an equivalent volume heat power of qA_w/N_{pw} is applied to all the N_{pw} particles in contact with the top wall with an area of A_w. Therefore, it seems that there is an equivalent surface heat flux of q applied on the top wall. Besides, periodic boundary conditions are imposed on the lateral surfaces of the assembly and no heat source is located in the pebble bed. In this situation, the effective heat flux through each cross-sectional surface perpendicular to z axis will be equal to a constant value of q when the bed reaches the steady thermal state (see Fig. 5(b)). Hence, the one-dimensional Fourier heat conduction law can be applied to calculate k_{eff} of the bed by

$$k_{eff} = -q/(\Delta T/\Delta z). \tag{28}$$

Fig. 5(c) shows the particle temperature against the particle position in z direction for the example case of a Li$_2$TiO$_3$ pebble bed filled with helium gas expected to be used in a fusion reactor [10]. The linear correlation between temperature and position in the bulk region indicates that thermal conductivity almost stays constant in the obtained temperature range and that the bulk region is homogeneous. Therefore, an equivalent parameter, k_{eff}, can be used to characterize the heat transfer. In this situation, $\Delta T/\Delta z$ can be obtained by linear regression of the temperature profile in the bulk region which is about 5 particle diameters from the wall in our model. According to this figure, for a heat flux of 100 W/m^2 at the top, the linear correlation for the temperature profile of the pebble bed is $T[°C] = 106z[m] + 424$. Therefore, the slope $\Delta T/\Delta z$ will be 106 °C/m. Based on Eq. (28), k_{eff} is estimated to be 0.94 W/(m K) for the Li$_2$TiO$_3$/He pebble bed at a mean temperature of 424 °C. The other results of the linear regression at different temperatures are shown in Table 1.

Alternatively, the effective thermal conductivity of the packed bed can also be explicitly expressed by the total effective heat conductance H_m (or H_{ij} in Eq. (2)) of all the thermal contacts considering the solid contact conduction, solid-fluid-solid conduction and radiation. Assuming that the heat transfer mechanisms from radiation and convection in voids (i. e., mechanisms (4) and (5) mentioned in Section 2.2) can be neglected, and that heat flow in packed beds with stagnant fluid only exists within the corresponding thermal contacts represented by double-cone zones, the volume average heat flux can be replaced by a sum over all the N_m contacts interior to the volume of the whole investigated bed V, i. e.

$$\bar{\boldsymbol{q}} = -\bar{\boldsymbol{k}}_{eff}\nabla T = \frac{1}{V}\int \boldsymbol{q}dV = \frac{1}{V}\sum_{m=1}^{N_m}\hat{\mathbf{n}}_{q,m}q_mA_mL_m, \tag{29}$$

where $\bar{\boldsymbol{k}}_{eff}$ is the volume average conductivity tensor, q_m, A_m and L_m denote the heat flux, effective heat transfer area and distance between the centroids of two particles in contact, respectively, and $\hat{\mathbf{n}}_{q,m}$ is the unit vector directed along heat flux.

Substituting Eq. (2) and $Q_m = q_mA_m$ into Eq. (29), and noting that in a thermal contact,

$$\Delta T \approx \hat{n}_{L,mx}L_m\frac{\partial T}{\partial x} + \hat{n}_{L,my}L_m\frac{\partial T}{\partial y} + \hat{n}_{L,mz}L_m\frac{\partial T}{\partial z}, \tag{30}$$
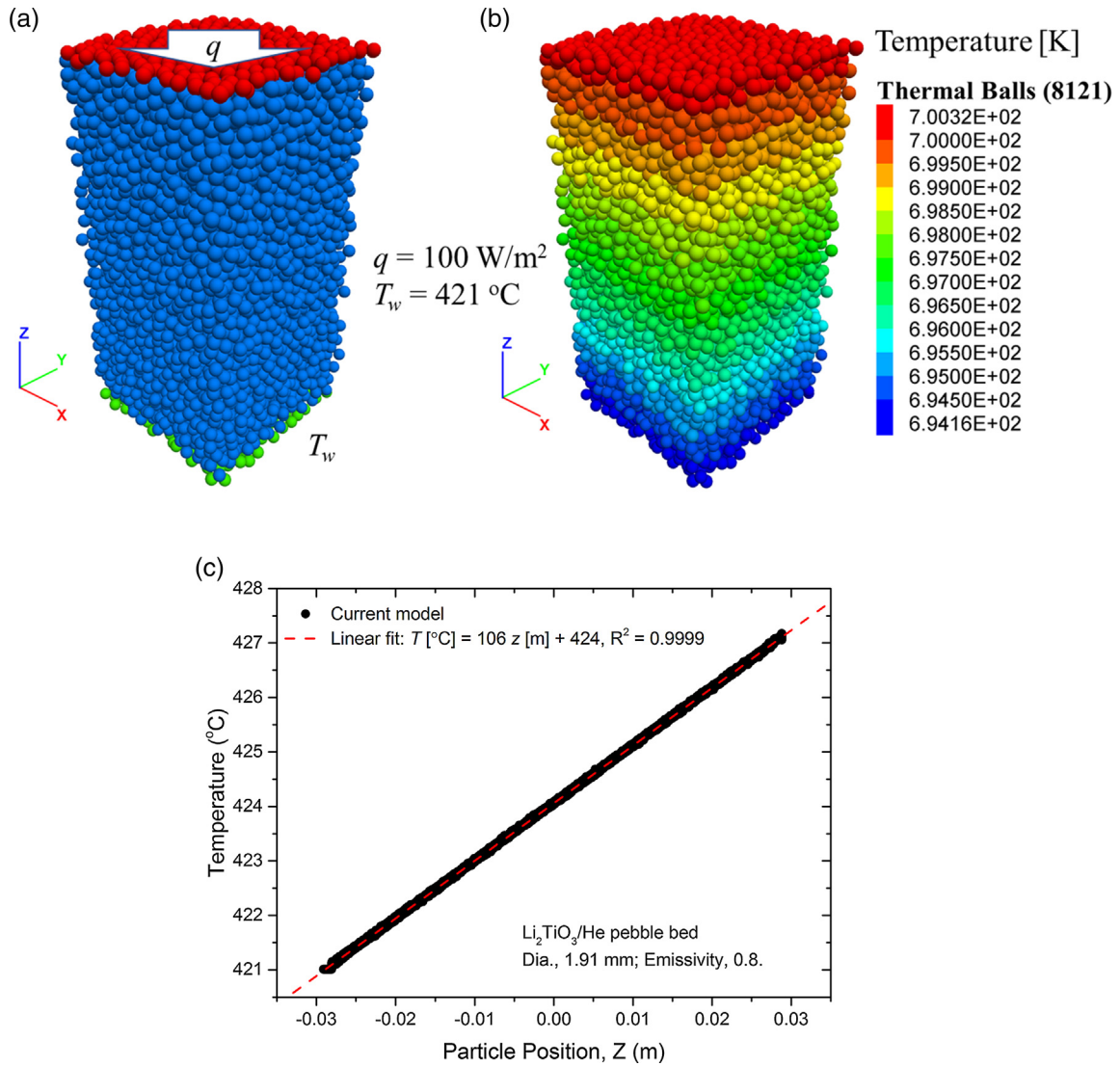
Fig. 5. Thermal DEM model for a Li$_2$TiO$_3$/He pebble bed (8121 particles with a diameter of 1.91 mm). (a) boundary conditions; (b) temperature field; (c) Particle temperature as a function of particle position z.

Table 1
Simulation results of a Li$_2$TiO$_3$ pebble bed with He gas.

T_w [°C]	q [W/m^2]	T-z linear regression ($T = a\,z + b$)			k_{eff} [W/(m K)]		
		a	b	R^{2a}	Eq. (28)	Eq. (32a) [$k_{eff}(k_{xx}/k_{yy}/k_{zz})$]	Measured [10]
421	100	106	424	0.9999	0.94	0.89(0.90/0.90/0.87)	1.00
521		99.7	524		1.00	0.92(0.93/0.93/0.90)	1.01
624		92.7	627		1.08	0.96(0.97/0.97/0.94)	1.11
670		89.5	672		1.12	0.98(0.99/0.99/0.96)	1.17
725		85.4	728		1.17	1.01(1.02/1.02/0.99)	1.16
773		81.8	776		1.22	1.04(1.05/1.05/1.02)	1.21

 a R^2 is the goodness of fit of the least method.

we have

$$\bar{\boldsymbol{k}}_{eff} = -\frac{1}{V}\sum_{m=1}^{N_m}H_m L_m^2 \hat{\boldsymbol{n}}_{q,m}^T \otimes \hat{\boldsymbol{n}}_{L,m}, \tag{31}$$

where $\hat{\boldsymbol{n}}_{q,m}^T$ is the transpose of $\hat{\boldsymbol{n}}_{q,m}$, $\hat{\boldsymbol{n}}_{L,m}$ is the unit vector directed from the lower-temperature particle centroid to the higher-temperature one, H_m is the effective heat conductance synonymous with H_{ij} in Eq. (2), and $\otimes$ represents the outer product of vectors. For

a pebble bed of spherical particles with an isotropic packing structure, $\hat{\boldsymbol{n}}_{q,m} = -\hat{\boldsymbol{n}}_{L,m}$. Therefore,

$$k_{eff} = \frac{k_{xx} + k_{yy} + k_{zz}}{3} = \frac{1}{3V}\sum_{m=1}^{N_m}H_m L_m^2. \tag{32a}$$

Combining Eq. (32a) and the equation for the bed volume $V = \frac{\pi}{6P_f}\sum_{p=1}^{N_p}d_p^3 = \frac{\pi N_p\langle d_p^3\rangle}{6P_f}$, leads to

$$k_{\text{eff}} = \frac{\bar{n}_m P_f}{\pi \langle d_p^3 \rangle} \langle H_m L_m^2 \rangle, \tag{32b}$$

where $\langle H_m L_m^2 \rangle$ denotes the average value of $H_m L_m^2$, and the packing factor P_f as well as the average coordination number, $\bar{n}_m = 2N_m/N_p$, which represents the average number of contacts with each individual particle, are two important parameters characterizing the packing structure of pebble beds. Therefore, Eqs. (31), (32a) and (32b) associate the effective thermal conductivity to the pebble bed packing structure. Furthermore, Eq. (31) is also suitable for anisotropic pebble beds with textures in the packing structure, for instance. Batchelor and O'Brien [29] and Shuo Zhao [36] also obtained similar equations by using a different approach on the basis of Batchelor and O'Brien's analytical model. These equations can give the effective thermal conductivity without the calculation of the temperature field, which significantly speeds up the calculation. However, for a two-way thermo-mechanical coupling problem involving the thermal expansion effect, the temperature field calculation is still necessary because the particle expansion cannot be determined without the temperature distribution. Further details related to the influence of the packing configuration on k_{eff} are reported in Section 3.2.1 for mono-sized pebble beds and in Section 3.1.2 for binary pebble beds.

The k_{eff} values calculated by employing Eq. (32a) for the Li$_2$TiO$_3$ pebble bed are also listed in Table 1. Both methods gives results that deviate by a maximum of ±16% from experimental data [10]. It is noted that Eq. (28) gives values very close to experimental measurements, whereas Eq. (32a) underestimates the measured values by up to about 16%.

3. Results and discussions

In this section, simulation cases for different packed beds have been performed in order to validate the current thermal DEM model by comparing the results with existing experimental data of mono-sized and multi-sized beds. After that, the model was further applied to analyze the heat flow distribution in packed beds and the influence of the packing structure and the effect of the mechanical load on the effective thermal conductivity. Some thermal properties used in the simulations are listed in Table 2.

3.1. Model validation

3.1.1. Validation for unitary pebble beds
As discussed above, the result predicted by the current model for the Li$_2$TiO$_3$ pebble bed where the thermal conductivity ratio k_s/k_f only varies from 6 to 10 is good. However, as reported by

Aichlmayr [13], the thermal conductivity ratio k_s/k_f for some investigated pebble beds can range from 0.1 to 10,000. Aichlmayr [13] has collected about 160 points of experimental data for a variety of bed materials from different studies [13,21,37,38], including river sand, glass, steel and aluminum as solid particles, and water, glycerol, air, helium and CO$_2$ as the fluid phase. Fig. 6 shows these measured data as well as the results of k_{eff} calculated by using Eqs. (28) or (32a) against the thermal conductivity ratio. In the current calculation, the example case is assumed to be a bed assembled from 1.0 mm pebbles in the presence of 0.1 MPa air. The bed temperature is 23 °C as most of the relevant experimental data are measured at room temperature. In addition, the air conductivity is fixed as a constant (0.0259 W/(m K)) while the solid conductivity is adjusted to obtain the different conductivity ratios corresponding to the experiments. Since the temperature is very low, the radiation part contributes less than 0.01% and thus can be neglected. Therefore, only the solid-fluid-solid conduction part and the solid contact conduction part are important in the present simulations. As shown in Fig. 6(a), both Eqs. (28) and (32a) give consistent results with a deviation less than 7%. Therefore, in the following discussion, only the results of Eq. (32a) are taken as the example. When the conductivity ratio is below unity, which means the solid conductivity is less than the fluid conductivity (for example, water-filled sand bed), our model predicts a lower k_{eff} than the measured data. This is because in such a situation, the low solid conductivity leads to a relatively high-temperature drop across the solid particle and thus the current assumption of an isothermal core within the pebble is no longer suitable. But for a high conductivity ratio larger than unity, which is more relevant for gas-filled pebble beds, our model matches the trend exhibited by the measured k_{eff} in a wide range. For the intermediate conductivity ratio range 1–5, $c = 0.6$ ($c = c_i = c_j$, see Eq. (14)) was found to be the best to fit the experimental data. Especially, with this value the predicted curve in Fig. 6(a) more or less passes through the point (1.0, 1.0), which is reasonable when the fluid and solid conductivities within the bed are equal. For the high conductivity ratio range 5–10,000, the calculated dimensionless effective conductivity k_{eff}/k_f agrees well with the experimental data and slight variations of the parameter c from 0.45 to 0.55 do not affect the results significantly, which confirms the suitability of the suggested value of 0.5 in the Cheng-Yu-Zulli model. Therefore, it is suggested that $c = 0.5$ for $5 < k_s/k_f < 10000$ and $c = 0.6$ for $1 < k_s/k_f < 5$.

In Fig. 6(a), the additional predicted data for pebble beds of 50 mm particles almost coincides with the data for 1 mm particles, which suggests, in the present case, the influence of the investigated particle size on the effective thermal conductivity can be negligible. This can be explained by Eqs. (31) or (32). In our model,

Table 2
Material thermal properties.

Material	Thermal conductivity (W/(m K))	Emissivity
Li$_2$TiO$_3$ [42]	$\frac{1-\varepsilon_0}{1+\beta\varepsilon_0}\left(4.77 - 5.11 \times 10^{-3}T + 3.12 \times 10^{-6}T^2\right)$ $\beta = 1.06 - 2.88 \times 10^{-4}T$, $0.07 \leqslant \varepsilon_0 \leqslant 0.27$, 300 K $\leqslant$ T $\leqslant$ 1050 K	0.8[b]
ZrO$_2$ [39][a]	$2.64 + 0.989 \times 10^{-3}T - 3.65 \times 10^{-6}T^2 + 1.67 \times 10^{-9}T^3$, 700 K $\leqslant T \leqslant$ 1300 K	$-0.323 + 3.61 \times 10^{-3}T - 4.55 \times 10^{-6}T^2 + 1.67 \times 10^{-9}T^3$, 700 K $\leqslant T \leqslant$ 1300 K
Graphite [20]	$73.8428 - 0.0898607T + 5.57553 \times 10^{-5}T^2 - 1.27420 \times 10^{-8}T^3$, 700 K $\leqslant T \leqslant$ 1900 K	$0.505586 + 7.92943 \times 10^{-4}T - 5.228643 \times 10^{-7}T^2$ $+1.10479 \times 10^{-10}T^3$, 700 K $\leqslant T \leqslant$ 1900 K
Beryllium [43]	$\frac{291(1-\varepsilon_0)}{1+3.7\varepsilon_0^2}\left(1 - 1.65 \times 10^{-3}T + 1.464 \times 10^{-6}T^2 - 5.125 \times 10^{-10}T^3\right)$, $0 \leqslant \varepsilon_0 \leqslant 0.8$, 300 K $\leqslant T \leqslant$ 873 K	0.6[c]
Air	$9.611 \times 10^{-3} + 6 \times 10^{-5}T$, T (K), 0.1 MPa	–
Helium [44]	$0.1448(T/273)^{0.68}\left[1 + 2.5 \times 10^{-3}P^{1.17}(T/273)^{-1.85}\right]$, T(K), P(MPa)	–

[a] Correlation fitted to data from Ref. [39].
[b] Estimated value.
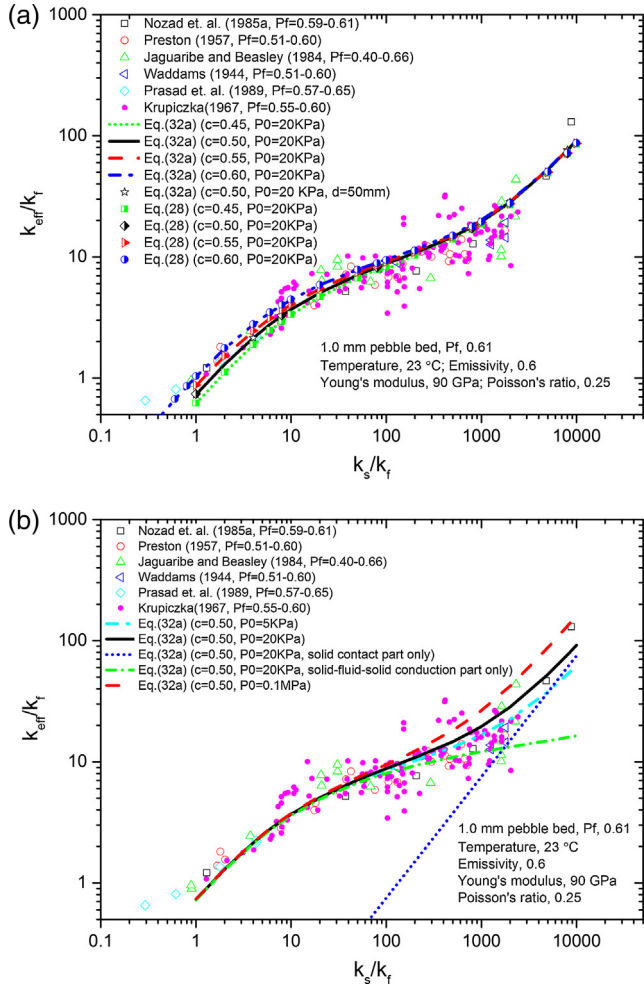[c] For unpolished surface.

Fig. 6. Validation for unitary pebble beds with different thermal conductivity ratios. (a) The determination of the fitting parameter c; (b) Influence of initial mechanical load P_0.

it is clear that the contact conductance and the solid-fluid-solid conduction conductance satisfy $H_{ij}^t \propto r_t \propto d_p$ and $H_{ij}^d \propto L_{ij} \propto d_p$, respectively, while for the radiation part, $H_{ij}^r \propto A_i \propto d_p^2$. Hence the total effective conductance $H_{ij} \propto \omega_1 d_p + \omega_2 d_p^2$. Considering $V \propto d_p^3$ and $L_m \propto d_p$, Eqs. (31) or (32) will lead to $k_{eff} \propto f(\omega_1) + f(\omega_2)d_p$. Therefore, k_{eff} should be almost consistent for different particle sizes when the second linear part given by the radiation can be neglected, as in the present case.

Fig. 6(b) shows the effective thermal conductivity affected by the initial mechanical load P_0. In these cases, the mechanical load is calculated by using the code of Chen [32] and fixed to P_0 during the thermal DEM simulation. The particle Young's modulus and Poisson's ratio are assumed to be 90 GPa and 0.25 (from Li_4SiO_4 material widely used in fusion blankets), respectively. It can be seen that in the lower conductivity ratio range $1 < k_s/k_f < 100$, the solid-fluid-solid conduction part absolutely dominates the total effective conductivity of the bed, while in the transition range $100 < k_s/k_f < 2000$, both conduction part and the contact part are important. In the higher conductivity ratio range $k_s/k_f > 2000$, comparing the contributions of the conduction part and the contact part, it is obvious that the contact part starts governing the total effective conductivity, and k_{eff} rises rapidly with the increasing mechanical load. For example, if the conductivity ratio is fixed at 2000, k_{eff}/k_f grows from 22.5 to 42.1 when the mechanical load

increases from 5 kPa to 0.1 MPa. The influence of mechanical load on k_{eff} will be further discussed in Section 3.2.3.

The current model reveals the contribution of the two conduction heat transfer mechanisms and works well for a wide range of conductivity ratios. However, on one hand, since k_{eff} is sensitive to the external mechanical load for pebble beds with high solid-to-fluid conductivity ratio, more exact experimental data with error bars are necessary to validate the current model. On the other hand, the radiation part cannot be verified by the above data because in these experiments the contribution of radiation part can be ignored. One possible way for the validation of the radiation part is to compare the calculated k_{eff} with the measured data of high-temperature pebble beds in a vacuum condition where the solid-fluid-solid conduction part has no contribution. Breitbach and Barthels [39] measured the effective thermal conductivity of a 45 mm ZrO_2 pebble bed and a 40 mm Graphite pebble bed under vacuum condition. Robold [19] also measured this for a 40 mm Graphite pebble bed. Their experimental data are plotted in Fig. 7. As shown by the dashed curves in the figure, the contact conduction part only contributes less than 1% to the total effective thermal conductivity indicated by the red solid line, so the radiation part dominates the heat transfer in both pebble beds. It can be seen that the calculated results match the experimental data within a deviation of ±30%. The effective thermal conductivity for both beds shows a significantly increasing tendency with rising
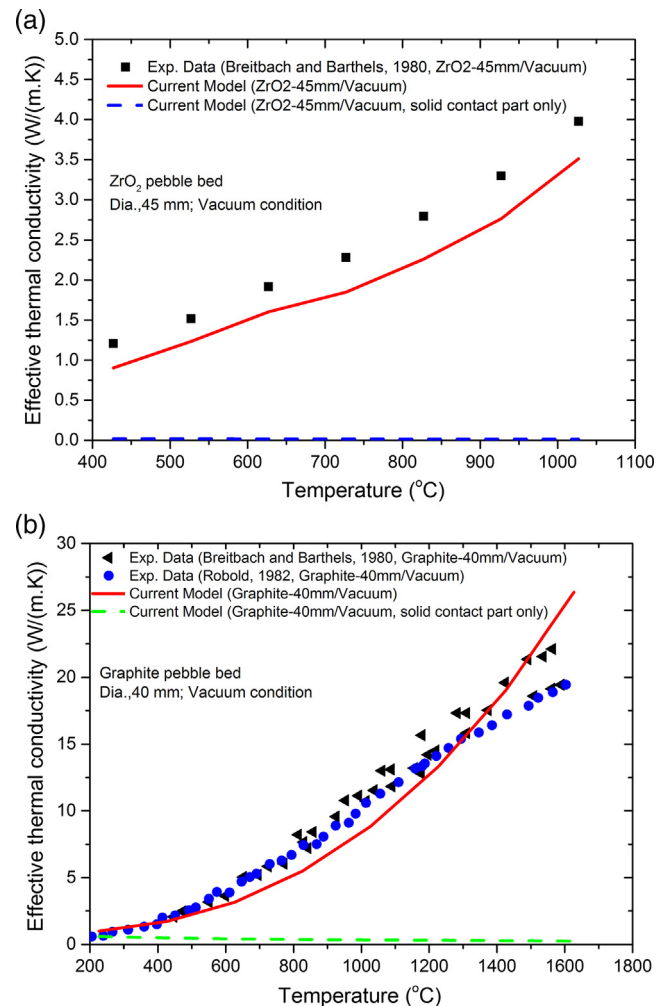

Fig. 7. Validation for unitary pebble beds at high temperature. (a) ZrO_2 pebble beds in vacuum condition; (b) Graphite pebble beds in vacuum condition.

temperature. However, in the temperature range of 400–1300 °C, the model underestimates the effective thermal conductivity with a deviation of up to −30%, but when the temperature grows beyond 1300 °C, the model overestimates the value by a deviation up to +30%, which means that the predictive capability is not exactly in accordance with the experiments. This is probably because the current model neglects the temperature variation inside the pebbles during the derivation of the radiation heat transfer model. Also, the long-range radiation [20] between two different Voronoi cells is not included in the current calculation. Further study is necessary to update the radiation part. But for many engineering purposes, including solid breeder pebble beds for fusion reactors, the contribution of the radiation heat transfer is not very significant [26]. Therefore, the accuracy of the present model will be sufficient for the time being.

3.1.2. Validation for pebble beds with different particle sizes or different materials

Particles in real packed beds are usually not equal-sized but have a size distribution. Besides, some mixed pebble beds consist of two or more components with different thermal properties [5]. In order to validate the current model for such situations, the predicted data were compared with experimental data from Okazaki et al. [8]. Okazaki et al. measured the effective thermal conductivity for binary mixtures of glass beads ($E_i = 88$ GPa, $v_i = 0.215$), acrylic resin ($E_i = 2.5$ GPa, $v_i = 0.4$) and copper ($E_i = 120$ GPa, $v_i = 0.34$) with a size ratio up to 2.82 at room temperature. The current results are reported in Fig. 8 where three graphs are presented. In these cases, the mechanical load is assumed to be 5 kPa. As shown in Fig. 8(a), for packed beds composed of two components with the same size distribution but different materials, effective thermal conductivities predicted by the current model are in agreement with those measured by Okazaki et al. and calculated by using the Cheng-Yu-Zulli model [23]. It is also observed that effective thermal conductivity increases with the increasing volume fraction of the particles with the higher thermal conductivity because they contribute more to k_{eff} compared to the particles with the lower thermal conductivity.

Fig. 8(b) gives the data for two cases of pebble beds with different diameters but the same material. In the two cases, the size ratio of the two components is about 1.69 and 2.82, respectively. The Cheng-Yu-Zulli model for mono-sized beds is not applicable now [23,28], but the current model still predicts values with a maximum deviation of ±15%. It is noted that in such cases the trend of the effective thermal conductivity is dependent on that of the packing factor. When the volume fraction of the large particle increases from zero to unity, both the packing factor and the effective thermal conductivity first grow to a peak and then drop to a lower value. Figs. 8(c) and 9 also show the results of two pebble beds with different diameters and different materials and the temperature distribution of two example cases, respectively. It can be seen that the trend of effective thermal conductivity is related to not only the packing factor but also the solid conductivity ratio of the large to small particles. The solid conductivity ratio seems to dominate the variation of the effective thermal conductivity, but the peak packing factor still leads to a small local fluctuation of k_{eff} at a volume fraction of about 0.6. For these mixed pebble beds, higher deviations are observed at some points, but still within ±15%. The deviation might partially be due to the different packing factors (shown in Fig. 8(c)) between experiments and simulation. Besides, the homogeneity in the mixed beds might also affect the measured k_{eff}.

As shown above, the current model demonstrates a good predictive capability for the binary mixtures when the size ratio reaches up to 2.8 as well as when the large-to-small particle
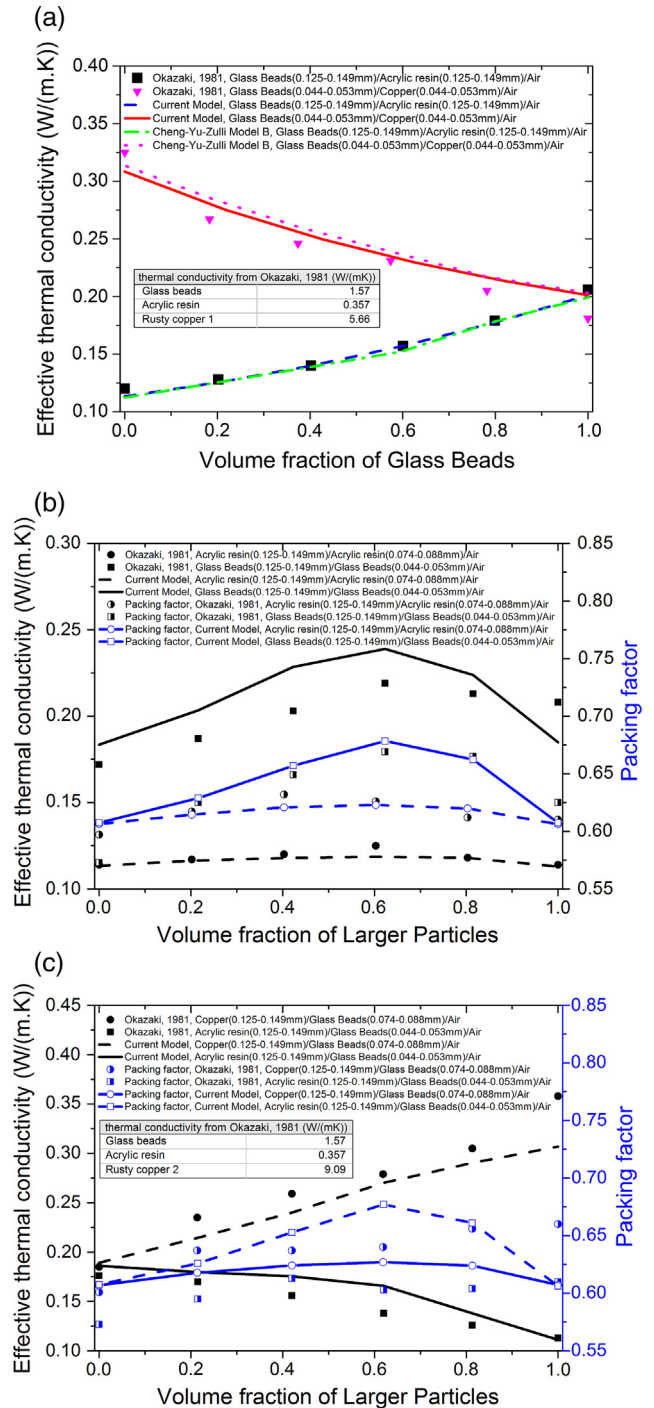

Fig. 8. Validation for pebble beds with different particle sizes and different materials. (a) pebble beds with the same size but different materials; (b) pebble beds with different sizes and the same material; (c) pebble beds with different sizes and different materials.

conductivity ratio varies from 0.23 to 5.8, but more measured data are still necessary to verify it for binary pebble beds with a higher size ratio and a wider solid conductivity ratio range.

3.2. Model application

3.2.1. Influence of packing structure on the effective thermal conductivity

The discussion in the last section indicates that the k_{eff} of binary mixtures is related to the packing structure parameters such as the
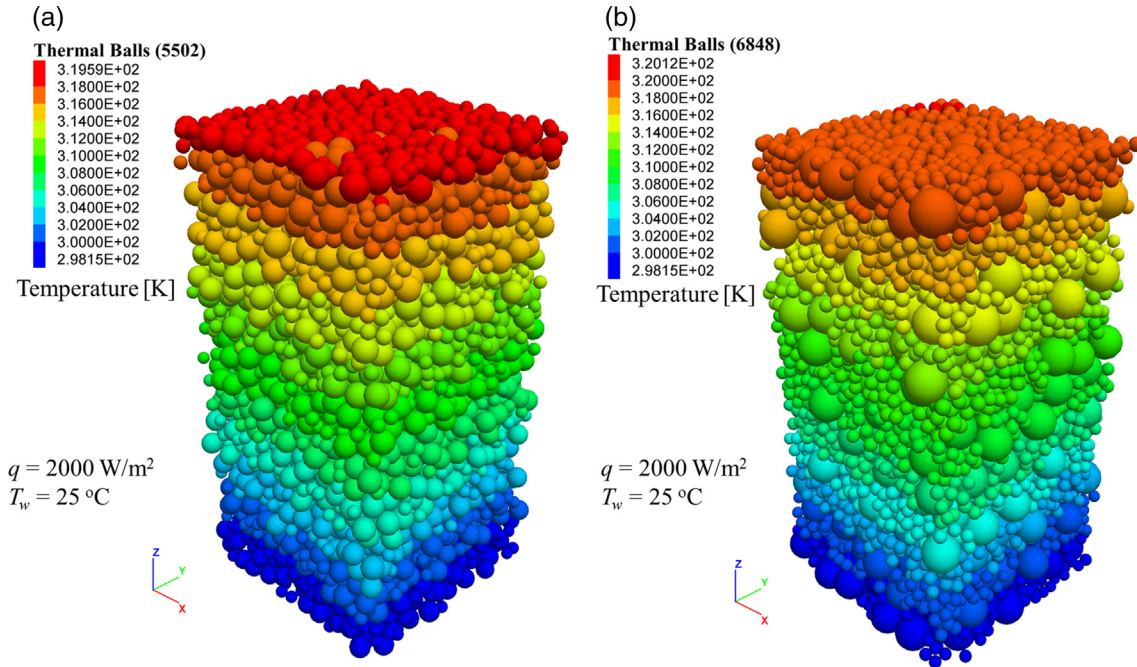
Fig. 9. Temperature profile of binary pebble beds. (a) Materials: Copper (0.125–0.149 mm)/Glass beads (0.074–0.088 mm)/Air; large particle volume fraction: 0.813; packing factor, 0.624; (b) Materials: Acrylic resin (0.125–0.149 mm)/Glass beads (0.044–0.053 mm)/Air; large particle volume fraction, 0.62; packing factor, 0.661.

packing factor and the volume fraction of each component. Additionally, in order to demonstrate the influence of the packing structure of unitary beds, the effective thermal conductivity for a Li_2TiO_3 pebble bed consisting of 1.91 mm particles with different packing structures is listed in Table 3. The considered packing structures are SC (simple cubic), RCP (random close packing), BCC (body centered cubic) and FCC (face centered cubic), respectively. Obviously, pebble beds of different packing structures have different values for k_{eff}. For the mono-sized bed with small mechanical load, most of the thermal contacts are nearly in point contact and about 84% contacts have a length of less than $1.1d_p$ for the current case of the Li_2TiO_3 pebble bed, which leads to $L_m \approx d_p$. Therefore, Eq. (32b) can be simplified as

$$k_{eff} \approx \frac{\bar{n}_m P_f}{\pi d_p} \bar{H}_m. \tag{33}$$

Eq. (33) further indicates that the k_{eff} of a mono-sized bed is proportional to a dimensionless quantity related to the packing structure, namely $\bar{n}_m P_f$, as well as to the effective heat conductance per unit length, $\bar{H}_m/d_p$. Given the equation for packed beds of spherical particles $P_f V = P_f \sum_{m=1}^{N_m} \frac{A_{n,m} L_m}{3} = \frac{\pi}{6} \sum_{p=1}^{N_p} d_p^3$ and the approximation

$L_m \approx d_p$, the average nominal area $\bar{A}_n$ for the mono-sized bed with small mechanical load can be estimated to be

$$\bar{A}_n \approx \frac{\pi d_p^2}{\bar{n}_m P_f} \tag{34}$$

Substitution of Eq. (34) into Eq. (33) yields

$$k_{eff} \approx \frac{d_p}{\bar{A}_n} \bar{H}_m \approx \frac{L_m}{\bar{A}_n} \bar{H}_m \overset{def}{=} k_m \tag{35}$$

Combination of Eqs. (35), (34) and (3) provides us with an estimated k_{eff} for a unitary bed without the DEM calculation. The results of k_m calculated by Eq. (35) and k_{eff} by the DEM simulation are listed in Table 3. They agree well with each other. This equation implies that one can estimate the effective thermal conductivity of the whole packed bed by the effective conductivity of one single contact within a unitary bed, which is reasonable because most of the thermal contacts in the mono-sized bed with small mechanical load have similar effective conductivities and thus the whole pebble bed has the same properties for all local contacts. This also explains why many cell-based theoretical models for the effective thermal conductivity prediction of mono-sized beds, such as the ZBS model [15] as well as Kunii and Smith model [14], obtain substantial success. Concerning a binary bed of different particle sizes

Table 3
Effective thermal conductivity of pebble beds with different packing structures.[a]

Packing Structure	Packing factor	Coordination number	k_{eff}[c] (W/(m K))	$\bar{H}_m$[d] (W/K)	k_m[e] (W/(m K))
SC	0.52 ($\pi/6$)	6	0.57	1.11×10^{-3}	0.58
RCP	0.604	9.7[b]	0.89	0.89×10^{-3}	0.87
BCC	0.68($\sqrt{3}\pi/8$)	8	0.88	0.92×10^{-3}	0.83
FCC	0.74($\sqrt{2}\pi/6$)	12	1.06	0.73×10^{-3}	1.09

[a] Results for 1.91 mm Li_2TO_3 pebble bed in the presence of helium (421 °C).
[b] Thermal contact statistics includes the area-/point- contact particle pairs, as well as the non-contacted particle pairs (because heat transfer exists in this situation). Therefore, it is larger than the coordination number defined by the mechanical contacts.
[c] Obtained by the current DEM simulation.
[d] Calculated by Eq. (3).
[e] By Eq. (35).

or different materials, the packing structure is complex, and each individual contact might have a unique effective conductivity, such that the cell-based theoretical models might predict inapplicable results. In such a situation, the present model can be a better choice.

3.2.2. Heat flow distribution

As the current numerical model is based on the heat transfer between pebble-scale Voronoi cells generated in the whole pebble bed assembly, it can be used to visualize the heat flow distribution.

Fig. 10(a) presents the angular distribution of the contact angle and the heat flow of a random 1.91 mm Li_2TiO_3/helium pebble bed at a temperature of 421 °C. Here, the contact angle φ is defined as the acute angle between the central axis of the corresponding contact and the global heat flux direction, namely the vertical direction in the assembly. In the present analysis, the probability density of the contact angle PDF_φ is obtained from

$$PDF_\varphi = \Delta N_{m\varphi}/(N_m \Delta \varphi), \tag{36}$$

where $\Delta N_{m\varphi}$ denotes the contact number falling in the contact angle range of $\varphi \sim \varphi + \Delta \varphi$, and N_m, which is the total contact number in the assembly, has been included in Eq. (36) as a normalizing factor to ensure the overall probability equals unity. Additionally, the average heat flow through a single thermal contact in φ direction is calculated by

$$Q_{m\varphi} = \Delta Q_\varphi/\Delta N_{m\varphi} \tag{37}$$

with the heat flow falling in the range of $\varphi \sim \varphi + \Delta \varphi$ computed by

$$\Delta Q_\varphi = \sum_{n=1}^{\Delta N_{m\varphi}} Q_{m\varphi,n}, \tag{38}$$

where $Q_{m\varphi,n}$ is the heat flow through the nth contact in $\varphi \sim \varphi + \Delta \varphi$ direction. The probability density of the total heat flow is therefore obtained from

$$PDF_{Q_\varphi} = \Delta Q_\varphi/(Q\Delta\varphi). \tag{39}$$

Here, Q is the total heat flow through all the thermal contacts in the assembly.

As shown in Fig. 10(a), the calculated probability density of the contact angle increases with rising angle and reaches a maximum value in the horizontal direction. The probability density of the contact angle PDF_φ is close to a sine-type distribution, which was also observed in Reimann's experiment by X-ray microtomography [40]. On the contrary, as indicated by the green dotted solid line, the normalized average contact heat flow through a single thermal contact decreases with rising angle and comes up to the maximum in the vertical direction, which is similar with a cosine-type distribution. The angular distribution of the heat flow through a single thermal contact can be explained by the heat conduction within the contact. The heat flow through the contact along φ direction can be estimated by Fourier's law

$$Q_{m\varphi} \approx -k_m A_m \frac{\Delta T}{L_m} = -k_m A_m \frac{\Delta T}{\Delta z} \cos \varphi. \tag{40}$$
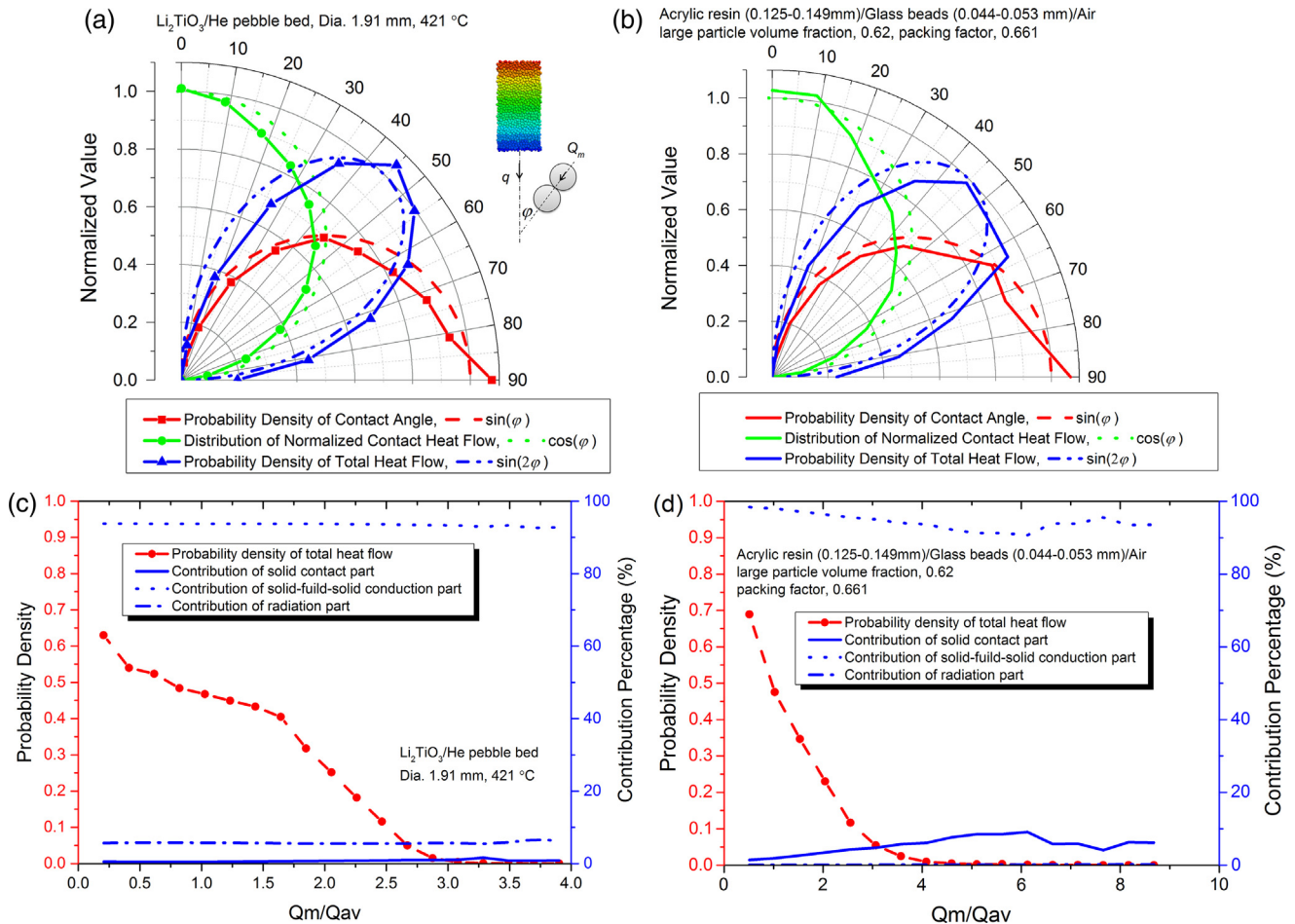

Fig. 10. Heat flow distribution in pebble beds. (a) and (b), Angular distribution of contact angle and heat flow for a mono-sized pebble bed and a mixed pebble bed; (c) and (d), Probability density distribution of dimensionless contact heat flow for a mono-sized pebble bed and a mixed pebble bed.

If fixed heat flux of q is defined in z direction for an isotropic pebble bed, applying Fourier's law for the whole assembly leads to $q = -k_{eff}\Delta T/\Delta z$. Using the above approximate formula $k_{eff} \approx k_m$ and combining these equations yields

$$Q_{m\varphi} \approx qA_m \cos\varphi. \tag{41}$$

As the effective heat transfer area in a contact (A_m) does not change too much for all the contacts in mono-sized beds, $Q_{m\varphi}$ through a contact will present cosine-type distribution.

Multiplying the probability density of contact angle and the related average heat flow through a single thermal contact results in the total heat flow in the corresponding contact angle direction. Therefore, given the above approximate sine-type distribution for the contact angle ($dN_{m\varphi} \approx N_m \sin\varphi d\varphi$), the amount of the total heat flow falling in the range of $\varphi \sim \varphi + d\varphi$ will be

$$dQ_\varphi = Q_{m\varphi}dN_{m\varphi} \approx \frac{1}{2}qA_mN_m \sin 2\varphi d\varphi. \tag{42}$$

This explains why the probability density of the total heat flow has a $\sin(2\varphi)$ -type distribution. This in turn indicates that the total heat flow mainly passes through the direction of 45°. But it is noted that in reality A_m and k_m also have a distribution. The heat flow is therefore deviates away from the standard regular distribution. As shown in Fig. 10(b), this deviation between them seems to be more obvious for a binary bed in which about 60% of the contacts are formed between two smaller particles and more than 30% contacts are between the larger and smaller particles.

The probability density distributions of the dimensionless contact heat flow, i.e. Q_m/Q_{av} ($Q_{av} = Q/N_m$ is the average heat flow for all the contacts), and the fraction of the three heat transfer mechanisms contributing to it are shown in Fig. 10(c) for a mono-sized and in Fig. 10(d) for a multi-sized bed. The distributions of Q_m/Q_{av} in both cases are different, although their angular distributions shown in Fig. 10 are similar. Concerning the contribution of the three heat transfer mechanisms, the solid-fluid-solid conduction dominates the heat transfer in both the mono-sized and the multi-sized bed by a fraction of more than 90%. The contact part and the radiation part only contribute less than 10% because the solid-to-fluid conductivity ratio and the temperature are not very high. It is noted that the contributions of radiation and contact part in the two cases are swapped, which is probably due to the different pebble sizes and different temperatures since packed beds of larger pebbles at higher temperature are more affected by radiation.

3.2.3. Influence of mechanical load on effective thermal conductivity

As discussed in Section 3.1.1 and shown in Fig. 6(b), a mechanical load has a significant influence on the effective thermal conductivity of pebble beds with high solid-to-fluid conductivity ratios. Reimann et al. [11,12] measured the effective thermal conductivity for a beryllium pebble bed which is a neutron multiplier for solid breeder blankets in fusion reactors. 0.8–1.2 mm beryllium particles of 98% theoretical density ($k_s = 177.9$ W/(m K)) and helium at room temperature (25 °C) and atmospheric pressure ($k_f = 0.154$ W/(m K))) compose the bed. Hence, the solid-to-gas conductivity ratio is about 1155. The pebble bed was compressed up to a maximum uniaxial mechanical load of 6 MPa and was then unloaded slowly to zero stress. Meanwhile the effective thermal conductivity and the strain-stress curve were measured during the quasi-static loading/unloading process. The numerical results of thermo-mechanical characteristics were calculated by using the mechanical DEM code of Chen [32] and the current thermal DEM code. Both the numerical results and Reimann's experimental data are shown in Fig. 11(a). The calculated strain-stress results are close to the observed data in the experiments during the loading
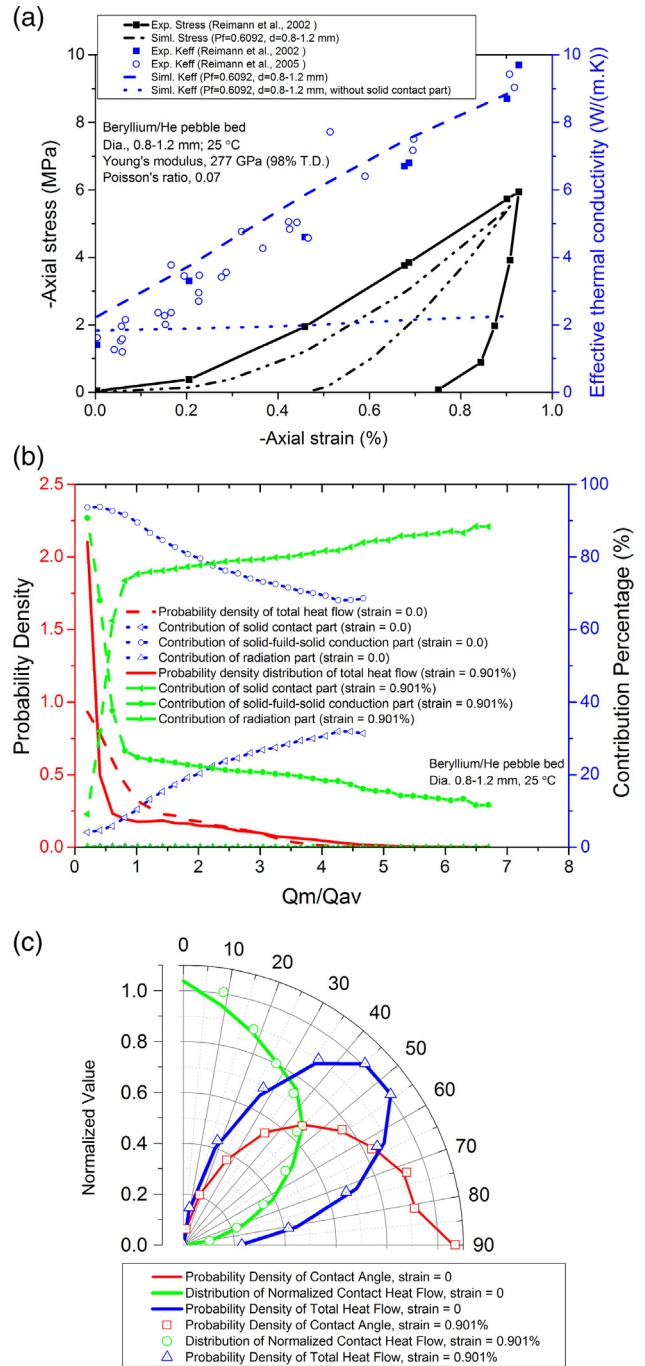

Fig. 11. Heat transfer characteristics of the beryllium pebble bed under mechanical load. (a) Effective thermal conductivity; (b) Probability density distribution of heat flow; (c) Angular distribution of contact angle and heat flow.

process while the simulations yielded less residual strain after the unloading process. Concerning the heat transfer characteristics, the calculated k_{eff} shows a dramatic linearly increasing trend when the strain rises, which was also observed in the experiments. However, the current numerical DEM model overpredicts k_{eff} by about 50% under the zero-stress state. This is probably because the effect of particle roughness is neglected in the present model. Particle roughness, on one hand, introduces plastic deformation on the surface of particles due to poor initial contact area while the bulk regions of the particles are still elastic, which is helpful to understand the missing residual strain in our model. On the other hand, if the mechanical load is small enough, poor initial contact area caused by particle roughness might result in a large thermal

resistance within the "contact regions" of contact pairs [41]. However, this thermal resistance will become smaller if the mechanical load increases. This explains why the thermal DEM model predicts k_{eff} better under a larger stress state. In view of that, further studies are necessary to evaluate the impact of particle roughness and the resulting interface resistance.

Fig. 11(a) also shows k_{eff} of the beryllium pebble bed without the contribution of the solid contact conduction. Due to the increase of the packing factor and the coordination number after loading up to 6 MPa, the contribution of the solid-fluid-solid conduction part and the radiation part only grows by 23.2%, while the total k_{eff} increases rapidly by 294%. This indicates that the mechanical load has a strong effect on the solid contact conduction which in turn dominates the overall behavior. As shown in Fig. 11(b), for the better conductive contacts with $Q_m/Q_{av} \geqslant 1$, the contribution of the contact part increases from below 30% to over 70% after the bed is loaded up to 6 MPa, while the contribution of the solid-fluid-solid conduction part decreases from over 70% to below 30%. This further confirms the dominant contribution of the contact part in the present bed under the mechanical load. However, the solid-fluid-solid conduction part still dominates the heat transfer in those less conductive contacts with $Q_m/Q_{av} < 0.5$, which in turn leads to the probability density peak of the contact heat flow in the corresponding range of Q_m/Q_{av}. Besides, results shown in Fig. 11(c) indicate that the uniaxial mechanical load has limited influence on the angular distribution of the contact angle and the heat flow. This is probably because the uniaxial stress in the present case is still not high enough to cause an obvious change of the angular distribution and the pebble bed might synchronously adjust the packing structure in three dimensions and partially distributes the uniaxial load in each contact direction.

4. Conclusions

In this paper, a thermal contact theory for the heat transfer between two adjacent spherical particles has been derived and applied for packed beds using the discrete element method. Radical Voronoi tessellation was used to generate a network of Voronoi cells for mono-sized and multi-sized beds and three heat transfer mechanisms, namely solid contact conduction, solid-fluid-solid conduction, and radiation were considered within each individual thermal contact. By comparison to existing experimental data for the effective thermal conductivity of mono-sized packed beds, the proposed thermal DEM model was proven effective in a wide range of solid-to-fluid conductivity ratios from 1.0 to 10,000. In addition, the model predicted correct effective thermal conductivities for mixed beds with a large-to-small particle size ratio up to 2.8 and a large-to-small particle conductivity ratios from 0.23 to 5.8.

By further application of the current structure-based model, the heat flow distributions and the influence of local packing structure on the macro thermal properties such as the k_{eff} were analyzed. Besides, it was also found that the k_{eff} of packed beds with a high conductivity ratio is significantly dependent on the external mechanical load, which indicated a strong thermo-mechanical coupling effect for such beds. Nevertheless, for a more accurate prediction of the coupled thermo-mechanical behavior, the implementation of the particle roughness effect and thermal expansion has to be taken into account in the future work. Besides, heat transfer mechanisms due to radiation between adjacent voids and convection should also be considered in the next step to estimate their effects.

Conflicts of interest

The authors declared that they have no commercial conflicts of interest with regard to this work.

References

[1] J.J. Lerou, G.F. Froment, Velocity, temperature and conversion profiles in fixed bed catalytic reactors, Chem. Eng. J. 32 (1977) 853–861.
[2] H. Bakhtiary-Davijany et al., Characteristics of an integrated micro packed bed reactor-heat exchanger for methanol synthesis from syngas, Chem. Eng. J. 167 (2011) 496–503.
[3] X. Yang et al., 3D DEM simulation and analysis of void fraction distribution in a pebble bed high temperature reactor, Nucl. Eng. Des. 270 (2014) 404–411.
[4] H. Wu et al., Numerical simulation of heat transfer in packed pebble beds: CFD-DEM coupled with particle thermal radiation, Int. J. Heat Mass Transf. 110 (2017) 393–405.
[5] S. Liu et al., Conceptual design of a water cooled breeder blanket for CFETR, Fusion Eng. Des. 89 (2014) 1380–1385.
[6] D. Carloni et al., Requirements for helium cooled pebble bed blanket and R&D activities, Fusion Eng. Des. 89 (2014) 1341–1345.
[7] S. Yagi, D. Kunii, Studies on effective thermal conductivities in packed beds, Am. Inst. Chem. Eng. 3 (1957) 373–381.
[8] M. Okazaki et al., Effective thermal conductivity for granular beds of various binary mixtures, J. Chem. Eng. Japan. 14 (1981) 183–189.
[9] M.D. Donne, G. Sordon, Heat transfer in pebble beds for fusion blankets, Fusion Technol. 17 (1990) 597–635.
[10] T. Hatano et al., Effective thermal conductivity of a Li2TiO3 pebble bed for a demo blanket, Fusion Sci. Technol. 44 (2003) 94–98.
[11] J. Reimann et al., Measurements of the Thermal Conductivity of Compressed Beryllium Pebble Beds (FZKA 7096), Karlsruhe, 2005.
[12] J. Reimann et al., Thermomechanics of solid breeder and Be pebble bed materials, Fusion Eng. Des. 61–62 (2002) 319–331.
[13] H.T. Aichlmayr, The Effective Thermal Conductivity of Saturated Porous Media, University Of Minnesota, 1999.
[14] D. Kunii, J.M. Smith, Heat transfer characteristics of porous rocks, Am. Inst. Chem. Eng. 6 (1960) 71–78.
[15] R. Bauer, E.U. Schluender, Effective radial thermal conductivity of packings in gas flow- 2. Thermal conductivity of the packing fraction without, GasFlow (1978).
[16] R.O.A. Hall, D.G. Martin, The thermal conductivity of powder beds. a model, some measurements on UO2 vibro-compacted microspheres, and their correlation, J. Nucl. Mater. 101 (1981) 172–183.
[17] C.T. Hsu et al., A lumped-parameter model for stagnant thermal conductivity of spatially periodic porous media, J. Heat Transfer 117 (1995) 265–269.
[18] P. Cheng, C.T. Hsu, The Effective stagnant thermal conductivity of porous media with periodic structures, J. Porous Media. 2 (1999) 19–38.
[19] W. Van Antwerpen et al., A review of correlations to model the packing structure and effective thermal conductivity in packed beds of mono-sized spherical particles, Nucl. Eng. Des. 240 (2010) 1803–1818.
[20] W. Van Antwerpen et al., Multi-sphere Unit Cell model to calculate the effective thermal conductivity in packed pebble beds of mono-sized spheres, Nucl. Eng. Des. 247 (2012) 183–201.
[21] I. Nozad et al., Heat conduction in multiphase systems - I: theory and experiment for two-phase systems, Chem. Eng. Sci. 40 (1985) 843–855.
[22] P. Adnani et al., Effective thermal conductivity of binary mixtures at high solid to gas conductivity ratios, Chem. Eng. Commun. 120 (1993) 45–58.
[23] G.J. Cheng et al., Evaluation of effective thermal conductivity from the structure of a packed bed, Chem. Eng. Sci. 54 (1999) 4199–4209.
[24] T.S. Yun, T.M. Evans, Three-dimensional random network model for thermal conductivity in particulate materials, Comput. Geotech. 37 (2010) 991–998.
[25] L. Chen et al., Investigation of effective thermal conductivity for pebble beds by one-way coupled CFD-DEM method for CFETR WCCB, Fusion Eng. Des. 106 (2016) 1–8.
[26] M. Moscardini et al., Discrete element method for effective thermal conductivity of packed pebbles accounting for the Smoluchowski effect, Fusion Eng. Des. 127 (2018) 192–201.
[27] Y. Gan et al., A Thermal discrete element analysis of EU solid breeder blanket subjected to neutron irradiation, Fusion Sci. Technol. 66 (2014) 83–90.
[28] G.J. Cheng, A.B. Yu, Particle scale evaluation of the effective thermal conductivity from the structure of a packed bed, Radiat. Heat Transf. Ind. Eng. Chem. Res. 52 (2013) 12202–12211.
[29] G.K. Batchelor, R.W. O'Brien, Thermal or electrical conduction through a granular material, Proc. Roy. Soc. London A Math. Phys Eng. Sci. 355 (1977) 313–333.
[30] Help documentation for PFC Version 5.0, 2016.
[31] H.W. Zhang, Q. Zhou, H.L. Xing, H. Muhlhaus, A DEM study on the effective thermal conductivity of granular assemblies, Powder Technol. 205 (2011) 172–183.

[32] L. Chen, Thermo-mechanical Study of Pebble Beds for Water Cooled Ceramic Breeder Blanket, Doctoral thesis, University of Science and Technology of China, 2017 (in Chinese)

[33] C.H. Rycroft, VORO++: a three-dimensional Voronoi cell library in C++, Chaos 19 (2009) 1–16.

[34] J.H. Zhou, A.B. Yu, Y.W. Zhang, A boundary element method for evaluation of the effective thermal conductivity of packed beds, J. Heat Transf. 129 (2007) 363–371.

[35] K.G. Gupta, Analytical and Numerical Evaluation of Configuration Factors in Radiation Heat Transfer, University of Ottawa, 1969.

[36] S. Zhao, Multiscale Modeling of Thermomechanical Properties of Ceramic Pebbles, Doctoral thesis, Karlsruhe Institute of Technology, 2010.

[37] E.F. Jaguaribe, D.E. Beasley, Modeling of the effective thermal-conductivity and diffusivity of a packed-bed with stagnant fluid, Int. J. Heat Mass Transf. 27 (1984) 399–407.

[38] V. Prasad et al., Evaluation of correlations for stagnant thermal conductivity of liquid-saturated porous beds of spheres, Int. J. Heat Mass Transf. 32 (1989) 1793–1796.

[39] G. Breitbach, H. Barthels, The radiant heat transfer in the high temperature reactor core after failure of the afterheat removal systems, Nucl. Technol. 49 (1980) 392–399.

[40] J. Reimann et al., X-ray tomography investigations on pebble bed structures, Fusion Eng. Des. 83 (2008) 1326–1330.

[41] M. Bahrami et al., Thermal joint resistances of nonconforming rough surfaces with gas-filled gaps, J. Thermophys. Heat Transf. 18 (2004) 326–332.

[42] S. Saito et al., Density dependence on thermal properties of Li2TiO3 pellets, J. Nucl. Mater. 253 (1998) 213–218.

[43] M.C. Billone et al., ITER Solid Breeder Blanket Materials Database, (1993).

[44] H. Ju, Thermal properties calculation procedures and data manual, Atomic Energy Press, 1990 (in Chinese).